Common-Mode EMI Analysis With Active CMV Cancellation in Neutral-Point-Less H-Type Inverter

Kangbeen Lee, *Student Member, IEEE*, Mikayla Benson, *Member, IEEE*, Xiaofeng Dong, *Member, IEEE*, Lifang Yi, *Member, IEEE*, Jinyeong Moon, *Senior Member, IEEE*, and Woongkul Lee, *Senior Member, IEEE*

***Abstract*—Pulse width modulated inverters utilizing wide bandgap devices enhance motor drive efficiency by enabling higher dc-link voltages and switching frequencies. However, these advantages also lead to increased common-mode electromagnetic interference (CM EMI) noise. Conventional two-level six-phase inverters aim to reduce CM EMI by canceling common-mode voltage (CMV), ideally achieving zero CMV. The effectiveness of this approach is, however, limited by CMV mismatch issues, such as desynchronization and variations in CMV rise times, under two-level operations. This article analytically and experimentally investigates the active CMV cancellation capability under three-level operation in a neutral-point-less H-type (NPL.H) nverter. Despite the challenges associated with CMV mismatches, the three-level operation of the NPL.H inverter enhances CMV cancellation capability across the entire frequency spectrum, as it reduces the maximum CMV level by 33% compared to the conventional inverter. Experimental results show a 21% reduction in CMV magnitude within the 300 kHz to 30 MHz range and a 50% decrease in peak-to-peak ground current for the NPL.H inverter compared to the conventional inverter. Furthermore, the NPL.H inverter achieves a 62% reduction in the increase of CM EMI noise when both the dc-link voltage and switching frequency are doubled, in comparison to the conventional inverter.**

***Index Terms*—Active common-mode voltage (CMV) cancellation, electromagnetic interference, multilevel inverter, neutral point less inverter, neutral-point-less H-type (NPL.H) inverter.**

I. Introduction

PULSEWIDTH modulated (PWM) inverters have been widely adopted in variable-speed drives with wide bandgap devices, such as SiC and GaN [1], [2]. They are considered key enablers for increasing dc-link voltage and switching frequency to enhance the efficiency and performance of motor drives. However, the magnitude of common-mode electromagnetic interference (CM EMI) noise tends to increase with higher dc-link voltage and switching frequency, primarily due to the elevated switching speed associated with these conditions. As a result, EMI filters and advanced inverter topologies capable of generating zero common-mode voltage (CMV) are receiving growing attention for their potential to reduce the sensitivity of CM EMI noise magnitude to variations in dc-link voltage and switching frequency, compared to conventional inverters.

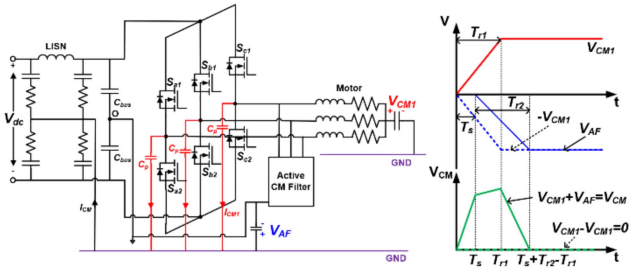

Fig. 1. Limitation of active CMV cancellation with desynchronization and slew rate difference between CMVs.

Analog EMI filters (AEFs) primarily employ operational amplifiers to inject compensation voltage into the circuit, thereby attenuating EMI [3], [4], [5], [6], [7], [8], [9], [10], [11], [12]. However, due to the inherent difficulty in synchronizing the compensation voltage with a CMV generated by electric drives, the CMV cancellation capability of AEFs is fundamentally limited by the constraints of analog circuitry. To overcome this synchronization challenge, digital EMI filters (DEFs) have been developed. DEFs digitize EMI signals, allowing for pre-compensation of desynchronization effects. This process involves signal acquisition via an analog-to-digital converter, digital signal processing, and re-injection of the compensated signal into the circuit through a digital-to-analog converter [13], [14]. By reconstructing a sensed CMV into a reverse-phase signal, DEFs achieve more effective mitigation of CM EMI noise than AEFs. However, their implementation is accompanied by inherent compromises, particularly a diminution in power density. As a topological solution, inverter topologies have been proposed in which two additional half-bridge structures are connected to the input of conventional inverters to achieve zero CMV generation [15], [16]. This approach had been improved from the concept of placing two additional switches in series with the direct current rails, allowing the inverter to be a floating during zero states to reduce CMV [17], [18], [19]. However, the adoption of complex PWM techniques becomes indispensable, leading to increased switching and conduction losses attributable to the inclusion of additional switch devices specifically intended for CMV mitigation. Therefore, six-phase inverter topologies have been considered to achieve

Received 18 February 2025; revised 21 May 2025; accepted 20 June 2025. Date of publication 23 June 2025; date of current version 5 August 2025. Recommended for publication by Associate Editor F. Dijkhuizen. *(Corresponding author: Kangbeen Lee.)*

Kangbeen Lee and Woongkul Lee are with the Elmore Family School of Electrical and Computer Engineering, Purdue University, West Lafayette, IN 47907 USA (e-mail: lee4097@purdue.edu).

Mikayla Benson is with the Electrical and Computer Engineering, Michigan State University, East Lansing, MI 48824 USA.

Xiaofeng Dong, Lifang Yi, and Jinyeong Moon are with the Electrical and Computer Engineering, Florida State University, Tallahassee, FL 32306 USA.

Color versions of one or more figures in this article are available at https://doi.org/10.1109/TPEL.2025.3582408.

Digital Object Identifier 10.1109/TPEL.2025.3582408

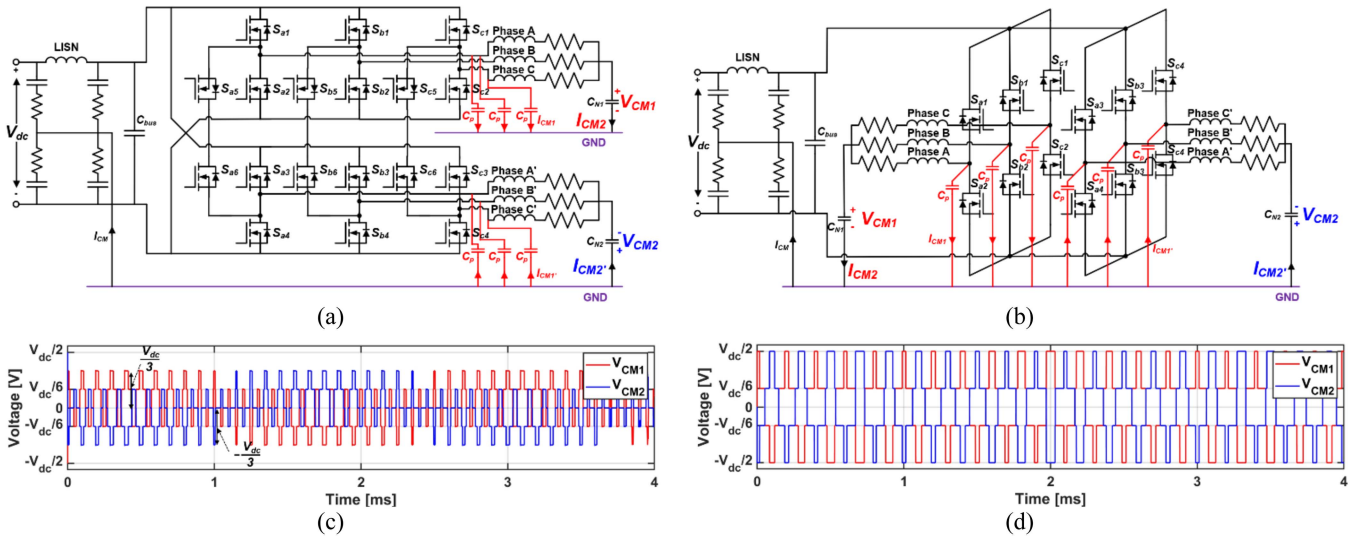

Fig. 2. Active CMV cancellation mechanism in (a) NPL.H inverter and (b) conventional inverter. Simulated CMV levels with (c) NPL.H inverter and (d) conventional inverter.

zero residual CMV (V_{CM}) by actively canceling CMVs generated by each three-phase set without EMI filters and switching devices dedicated solely to CMV reduction. A dual three-phase (conventional) inverter, which consists of two standard two-level inverters, has been experimentally verified to reduce the magnitude of CMV, resulting in a corresponding decrease in CM EMI noise magnitude [20], [21]. Similarly, a balanced inverter using nine switches has been studied to achieve active CMV cancellation, yielding lower CM EMI noise magnitudes compared to conventional two-level inverters [22], [23], [24], [25].

Although active CMV cancellation solutions are designed to achieve zero V_{CM}, mismatch challenges between CMVs hinder an ideal cancellation. The challenges are due to the skewing effect caused by desynchronized gate signals between switches and the slew rate disparity effect induced by power loop stray inductances, both of which diminish the cancellation capability, as depicted in Fig. 1 [10], [11], [12], [26], [27]. As a result, the magnitude of CM EMI noise inevitably increases with higher dc-link voltage and switching frequency. To mitigate the limitation caused by the skewing and disparity effect between CMVs, reducing CMV levels is necessary to achieve effective active CMV cancellation. Since a three-level operation with active CMV cancellation capability generate CMV magnitudes as 0, $\pm V_{\mathrm{dc}}/6$, and $\pm V_{\mathrm{dc}}/3$, which is reduced by 33% at the maximum level compared to the two-level inverter, the measured CM EMI noise magnitudes across various operating conditions are noticeably lower than those in two-level inverters [28], [29]. However, these studies lack analytical explanations regarding active CMV cancellation in relation to the mismatch challenges, as well as an experimental validation of its impact on CM EMI noise magnitude.

This article investigates the active CMV cancellation capability in a three-level operation through analytical and experimental validation. The three-level operation is implemented using a neutral-point-less H-type (NPL.H) inverter, as outlined in [30], [31], and [32]. To examine the impact of mismatch challenges on active CMV cancellation, the spectral envelopes of CMV in the NPL.H inverter are analyzed to determine the V_{CM} magnitude across the frequency spectrum resulting from the three-level operation. Additionally, time and frequency-domain analyses, utilizing measured CMV and ground current, are performed to explore the effect of dc-link voltage and switching frequency on CM EMI noise magnitude in the NPL.H inverter. To verify the advantages of active CMV cancellation in the three-level operation of the NPL.H inverter, comparisons with the conventional inverter are made through both analytical and experimental validations.

II. Active CMV Cancellation Capability Investigation in NPL.H Inverter

The NPL.H inverter, as depicted in Fig. 2(a), utilizes 18 active switches with a single dc-link capacitor configuration that eliminates the neutral current. As a thorough investigation of operation principal of the NPL.H inverter in [30], [31], and [32], four switching states are implemented in a phase leg (i.e., PN, NP, ZZ(+), and ZZ(-)).The PN and NP states require three switches to be in the on-state to achieve each voltage level, while the ZZ state requires only two switches for three-level operations with three-phase legs. The NPL.H inverter utilizes conventional three-phase multicarrier PWM techniques, with S_1/S_4 and S_2/S_3 having the same and synchronized PWM signals and S_5/S_6 being the complementary signals of the previous sets.

The NPL.H inverter generates 27 voltage vectors identical to those of conventional MLI topologies with three-phase legs. The switching states consist of zero, small, medium, and large vectors with CMV levels of 0, $\pm V_{\mathrm{dc}}/6$, $\pm V_{\mathrm{dc}}/3$, and $\pm V_{\mathrm{dc}}/2$, respectively. The NPL.H inverter generates two equal and opposite CMVs due to the identical and opposing output voltages in each three-phase leg, which result from the two sets of symmetrical windings being series-connected with opposite polarities in the stator. The simulated CMVs by LTspice software, observed as 0, $\pm V_{\mathrm{dc}}/6$, and $\pm V_{\mathrm{dc}}/3$ with phase disposition space vector PWM (PD SVPWM), cancel each other out, as illustrated in Fig. 2(c).

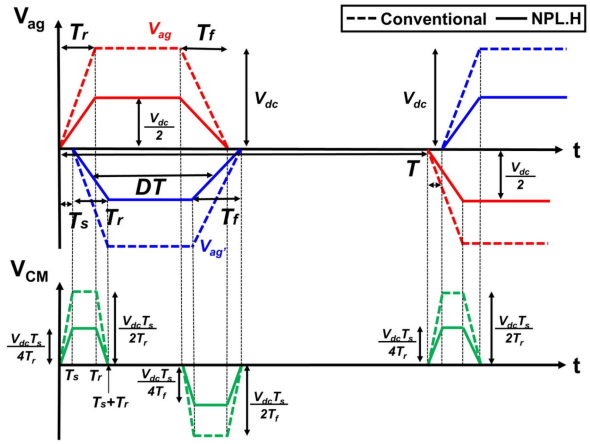

Fig. 3. Calculated V_{CM} considering skewing effect with each one phase-leg output voltage of conventional and NPL.H inverters.

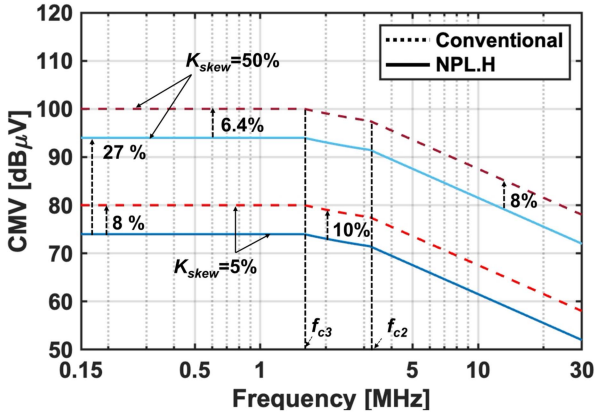

Fig. 4. Skewing impact on spectral envelope of V_{CM} in each inverter when K_{skew} varies 5% and 50% at $T_r = 100$ ns, $T_f = 200$ ns, $V_{\mathrm{dc}} = 200$ V, and $f_s = 5$ kHz.

The effectiveness of active CMV cancellation is affected by mismatch challenges, such as skewing and differences in slew rates between CMVs. To assess the impact of each mismatch factor on active CMV cancellation, the spectral envelope of V_{CM} is presented in this section. Since the V_{CM} spectrum of the three-phase legs is identical with the CMV spectrum of a single-phase leg, as verified in previous studies [22], [26], [27], this article focuses on analyzing CMV behavior within a phase leg. The active CMV cancellation capability of the NPL.H inverter is validated by comparing the CMV spectral envelope, considering mismatch challenges, with that of the conventional inverter, as shown in Fig. 2(b). The CMVs for the conventional inverter are estimated as $\pm V_{\mathrm{dc}}/6$ and $\pm V_{\mathrm{dc}}/2$, based on the averaged output voltages of each phase leg switching between V_{dc} and zero relative to ground, as shown in Fig. 2(d).

A. Timing Mismatch: Skewing Effect

The output voltages generated in the NPL.H inverter and conventional inverter cannot be perfectly canceled in actual operations because of the skewing time made by desynchronized gate signals between switches, as shown in Fig. 3. This discrepancy between the output voltages is attributed to differences in a rise time (T_r) and a fall time (T_f) of output voltages, a fixed duty ratio (D), a switching cycle period (T), and a skewing time (T_s) between the output voltages in a phase leg. The output voltages of the NPL.H inverter and conventional inverter can be estimated using asymmetrical trapezoids, as depicted with dashed and solid lines in Fig. 3, respectively. The maximum magnitude of CMV in NPL.H inverter are observed as $V_{\mathrm{dc}}T_s/2\min(T_r, T_f)$, which is half of the magnitude of CMV in the conventional inverter. These trapezoids serve as the fundamental components for constructing the CMV waveform.

With the assumption that T_r and T_f are smaller than DT and that T_r is smaller than T_f, the CMV spectral upper boundary of the nth-order harmonic is determined by Fourier series (1) gained by averaging output voltages, presented at the bottom of the next page. It is crucial to ascertain the $S(n)$ peaks while adjusting n.

In the high-frequency region (i.e., with a large n), the upper boundary of $S(n)$ in the NPL.H inverter takes place when $e^{-j2n\pi T_s/T}$, $e^{-j2n\pi T_r/T}$, $e^{-j2n\pi T_f/T}$, and $e^{-jn\pi(2DT+T_r-T_f)/T}$ equals -1

$$S(n)_h = \frac{V_{\mathrm{dc}}T}{2n^2\pi^2}\left(\frac{1}{T_r}+\frac{1}{T_f}\right) = \frac{V_{\mathrm{dc}}f_s}{2\pi^2 f^2}\left(\frac{1}{T_r}+\frac{1}{T_f}\right), \tag{2}$$

where V_{dc} and f_s present dc-link voltage and switching frequency, respectively. f is the x-axis of the frequency spectrum, and n is the harmonic order number such that f equals n times f_s.

As n decreases, the term addressing the skewing effect, $e^{-j2n\pi T_s/T}$, will not be able to reach -1 first because it is assumed that T_s is smaller than T_r. Therefore, the following approximation can be applied as

$$e^{-j2n\pi T_s/T} \approx 1 - \frac{j2n\pi T_s}{T}. \tag{3}$$

The upper bound of the spectral envelope for the high-mid frequency range can be approximated, as

$$S(n)_{h-m} = \frac{V_{\mathrm{dc}}T_s}{2n\pi}\left(\frac{1}{T_r}+\frac{1}{T_f}\right) = \frac{V_{\mathrm{dc}}T_s f_s}{2\pi f}\left(\frac{1}{T_r}+\frac{1}{T_f}\right). \tag{4}$$

The first corner frequency (f_{c1}) is calculated, as

$$f_{c1} = \frac{1}{\pi T_s}. \tag{5}$$

As n further decreases, $e^{-j2n\pi T_r/T}$ is not able to reach -1

$$e^{-j2n\pi T_r/T} \approx 1 - \frac{j2n\pi T_r}{T}. \tag{6}$$

The upper bound of the spectral envelope for the midfrequency range can be approximated, as

$$S(n)_m = \frac{V_{\mathrm{dc}}T_s f_s}{2\pi T_f f}\left(1+\pi T_f f\right). \tag{7}$$

The second corner frequency (f_{c2}) in the midfrequency range is calculated, as

$$f_{c2} = \frac{1}{\pi T_r}. \tag{8}$$

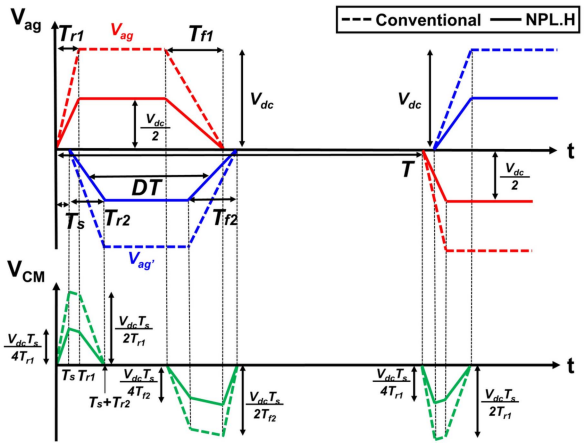

Fig. 5. Calculated V_{CM} considering both skewing and disparity effect with each one phase-leg output voltage of conventional and NPL.H inverters.

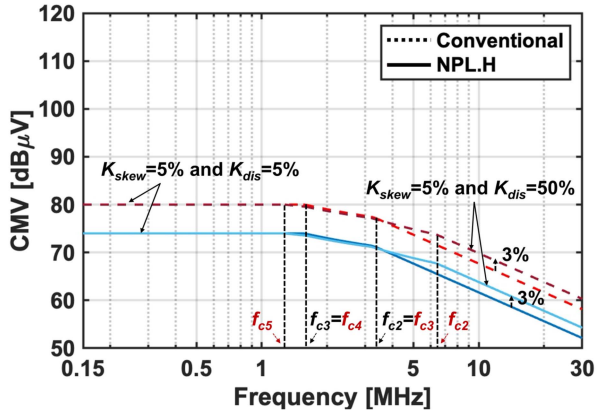

Fig. 6. Disparity impact on spectral envelope of V_{CM} in each inverter when K_{dis} varies 5% and 50% at $T_r = 100$ ns, $T_f = 200$ ns, $V_{\mathrm{dc}} = 200$ V, and $f_s = 5$ kHz.

After consecutive calculation, in the low-frequency range, the magnitude is bounded by the f_s and T_s as

$$S(n)_l = \frac{V_{\mathrm{dc}} T_s f_s \left| e^{-j\pi(2DT+T_r-T_f)/T} - 1 \right|}{2}. \tag{9}$$

Therefore, the third corner frequency (f_{c3}) in the low-frequency range is calculated, as

$$f_{c3} = \frac{1}{\pi T_f}. \tag{10}$$

Since the output voltage magnitude in one-phase leg of the conventional inverter is observed to be twice that of the NPL.H inverter, the spectral envelopes in the conventional inverter are obtained with the same corner frequencies, as

$$S(n)_h = \frac{V_{\mathrm{dc}} T}{n^2\pi^2}\left(\frac{1}{T_r}+\frac{1}{T_f}\right) = \frac{V_{\mathrm{dc}} f_s}{\pi^2 f^2}\left(\frac{1}{T_r}+\frac{1}{T_f}\right) \tag{11}$$

$$S(n)_{h-m} = \frac{V_{\mathrm{dc}} T_s}{n\pi}\left(\frac{1}{T_r}+\frac{1}{T_f}\right) = \frac{V_{\mathrm{dc}} T_s f_s}{\pi f}\left(\frac{1}{T_r}+\frac{1}{T_f}\right) \tag{12}$$

$$S(n)_m = \frac{V_{\mathrm{dc}} T_s f_s}{\pi T_f f}\left(1+\pi T_f f\right) \tag{13}$$

$$S(n)_l = V_{\mathrm{dc}}\, T_s f_s \left| e^{-j\pi(2DT+T_r-T_f)/T} - 1 \right|. \tag{14}$$

By utilizing the spectral envelopes from each inverter, a parametric analysis is conducted to investigate an impact of skewing effect on the spectral envelopes in each inverter. The skewing ratio defined, as

$$K\mathrm{skew}\ (\%) = \frac{T_s}{T_r} \times 100 \tag{15}$$

is utilized in this article to quantify and compare the degree of the skewing effect. The skewing ratios are addressed as 5% and 50% with baseline drive parameters (i.e., $T_r = 100$ ns, $T_f = 200$ ns, $V_{dc} = 200$ V, and $f_s = 5$ kHz).

Since the magnitude of the spectral envelope of V_{CM} in the low frequency band is bounded by T_s at the same V_{dc} and f_s, an elevation of K_{skew} increases the magnitude in the frequency band (< 1.6 MHz (i.e., f_{c3})) in both inverters, as shown in Fig. 4. The magnitude with $K_{\mathrm{skew}} = 50\%$ in the NPL.H inverter presented by the blue solid line leads to a 27% elevation in the band compared to that with $K_{\mathrm{skew}} = 5\%$ presented by the black solid line. In addition, across the entire frequency band, the conventional inverter produces a CMV magnitude up to 10% higher than the NPL.H inverter as compared between the dash and solid lines in Fig. 4.

B. Slew Rate Mismatch: Disparity Effect

The slew rate difference between output voltages induced by power loop stray inductances also affects the active CMV cancellation capability, as shown in Fig. 5, each spectral envelope from the inverters considering both skewing and slew rate disparity is investigated with disparity ratio defined, as

$$K\mathrm{dis}\ (\%) = \frac{T_{r1}-T_{r2}}{T_{r1}} \times 100. \tag{16}$$

The differences between T_{r1} and T_{r2} and T_{f1} and T_{f2} of output voltages are addressed to derive the analytical expression for V_{CM}. Since T_s, T_{r1}, T_{r2}, T_{f1}, and T_{f2} are interchangeable in all the equations, it is assumed that $T_s < T_{r1} < T_{r2} < T_{f2} < T_{f1}$ in this section for simplicity. Although the V_{CM} waveforms exhibit different magnitudes at the corners due to the disparity effect, they are approximated as trapezoidal waveforms with maximum magnitudes when deriving the spectral envelopes of V_{CM}. This assumption results in negligible error, as T_s, T_{r1}, T_{r2}, T_{f1}, and T_{f2} are short. The spectral envelope of V_{CM} considering both skewing and slew rate disparity effect for the NPL.H inverter

$$S(n) = \left| \frac{TV_{\mathrm{dc}}}{8} \left(\frac{T_f\left(1-e^{-\frac{j2n\pi T_r}{T}}\right)+T_r\left(e^{-\frac{j2n\pi T_f}{T}}-1\right)e^{-\frac{jn\pi\left(2DT+T_r-T_f\right)}{T}}}{n^2\pi^2 T_r T_f} \right) \times \left(1-e^{-\frac{j2n\pi T_s}{T}}\right) \right| \tag{1}$$

can be derived after heavy calculation, as

$$S(n)_{h1} = \frac{V_{\rm dc} f_s}{4\pi^2 f^2}\left(\frac{1}{T_{r1}} + \frac{1}{T_{f1}} + \frac{1}{T_{r2}} + \frac{1}{T_{f2}}\right) \tag{17}$$

$$S(n)_{h2} = \frac{V_{\rm dc} T_s f_s}{4\pi f}\left(\frac{1}{T_{r1}} + \frac{1}{T_{f1}} + \frac{1}{T_{r2}} + \frac{1}{T_{f2}}\right) \tag{18}$$

$$S(n)_{m1} = \frac{V_{\rm dc} T_s f_s}{4\pi f}\left(\frac{1}{T_{f1}} + \frac{1}{T_{r2}} + \frac{1}{T_{f2}} + \pi f\right) \tag{19}$$

$$S(n)_{m2} = \frac{V_{\rm dc} T_s f_s}{4\pi f}\left(\frac{1}{T_{f1}} + \frac{1}{T_{f2}} + 2\pi f\right) \tag{20}$$

$$S(n)_{l1} = \frac{V_{\rm dc} T_s f_s}{4\pi f}\left(\frac{1}{T_{f1}} + 3\pi f\right) \tag{21}$$

$$S(n)_{l2} = V_{\rm dc}\, T_s f_s. \tag{22}$$

The corresponding corner frequencies are given as

$$f_{c1} = \frac{1}{\pi T_s} \tag{23}$$

$$f_{c2} = \frac{1}{\pi T_{r2}} \tag{24}$$

$$f_{c3} = \frac{1}{\pi T_{r1}} \tag{25}$$

$$f_{c4} = \frac{1}{\pi T_{f1}} \tag{26}$$

$$f_{c5} = \frac{1}{\pi T_{f2}}\,. \tag{27}$$

The spectral envelope of $V_{\rm CM}$ in the conventional inverter shows double the magnitude compared to the NPL.H inverter, while maintaining identical corner frequencies as the conventional inverter.

By utilizing the spectral envelopes from each inverter, a parametric analysis is conducted to investigate an impact of disparity effect on the spectral envelopes in each inverter with $K_{\rm dis} = 5$ and 50% and a fixed $K_{\rm skew} = 5\%$. The five corner frequencies are observed with the disparity effect, as shown in Fig. 6. Since the magnitude of $V_{\rm CM}$ is bounded by $V_{\rm dc}$, f_s, and T_s in the frequency band [$<$ 1.3 MHz (i.e., f_{c5})], the disparity effect does not significantly change the magnitude in the low frequency. It is also observed that the envelope magnitude with $K_{\rm dis} = 50\%$ drawn by the blue line increases up to 3% compared to that with $K_{\rm dis} = 5\%$ drawn by the black line in the frequency band ($>$ 3.2 MHz (i.e., f_{c3})).

C. Modulation Index Impact on Spectral Envelope

The preceding analysis is conducted on the fixed duty cycle CMV waveforms of the NPL.H inverter. However, due to the modulation technique utilized, the actual output voltages of the inverters feature a varying duty cycle. This section investigates the impact of the modulation index on the analytical spectral envelope of V_{CM} in the NPL.H inverter, considering only the skewing effect, which has a greater influence than the disparity effect, as demonstrated in Section II-A and Section II-B. To extend the previous analysis, the duty cycle with SVPWM leads to the modified spectral amplitude of the total CMV of the NPL.H inverter, as presented by

$$Dm = \frac{1}{2} + M_0\left\{\sin\left(\frac{2\pi\,(m-1)}{m_s}\right) + \frac{1}{6}\sin\left(\frac{6\pi\,(m-1)}{m_s}\right)\right\} \tag{28}$$

where M_0 is the modulation index between 0 and 1 in an ideal case, m indicates the order of the switching period, m_s is defined as f_s/f_u, and f_u is a fundamental frequency. To reorganize the spectral envelope, the function associated with D_m in the spectral envelope of $V_{\rm CM}$ with the NPL.H inverter is defined as

$$M = \sum_{m=0}^{m_s-1} e^{-j2k\pi M_0\left(\sin\left(\frac{2\pi m}{m_s}\right)+\frac{1}{6}\sin\left(\frac{6\pi m}{m_s}\right)\right)}/m_s \tag{29}$$

where k is the harmonic number. It is bounded by 1

$$0 < |M| \le 1. \tag{30}$$

Since the approximated spectral envelope of $V_{\rm CM}$ of the NPL.H inverter considering the term of M, the upper boundaries in different frequency regions are simplified

$$S(k)_{\rm high} = \frac{V_{\rm dc} T}{2k^2\pi^2}\left(\frac{1}{T_r} + \frac{|M|}{T_f}\right) = \frac{V_{\rm dc} f_s}{2\pi^2 f^2}\left(\frac{1}{T_r} + \frac{|M|}{T_f}\right) \tag{31}$$

$$S(k)_{\rm high-mid} = \frac{V_{\rm dc} T_s}{2k\pi}\left(\frac{1}{T_r} + \frac{|M|}{T_f}\right) = \frac{V_{\rm dc} T_s f_s}{2\pi f}\left(\frac{1}{T_r} + \frac{|M|}{T_f}\right) \tag{32}$$

$$S(k)_{\rm mid} = \frac{V_{\rm dc} T_s f_s}{2\pi T_f f}\,(|M| + \pi T_f f) \tag{33}$$

$$S\,(f_s) = \frac{V_{\rm dc} T_s f_s}{2}\left|e^{-\frac{j\pi\left(T+T_r-T_f\right)}{T}} M - 1\right|. \tag{34}$$

The spectral envelope of $V_{\rm CM}$ with the conventional inverter shows double the magnitude compared to the NPL.H inverter with the same corner frequencies, as verified in previous sections.

The spectral envelopes of $V_{\rm CM}$ of each inverter have two boundaries depending on the modulation index. While the upper bound of spectral envelope of $V_{\rm CM}$ with the NPL.H inverter at the baseline parameters increases up to 6.8% in the frequency band ($< f_{c3}$), it remains at least 2.7% below than that with the conventional inverter across the entire frequency band, as illustrated in Fig. 7.

These investigations into the effects of skewing and disparity on V_{CM} in each inverter with active CMV cancellation capability reveals four key findings. First, the NPL.H inverter reduces the spectral envelope magnitude of $V_{\rm CM}$ in the whole frequency band compared to the conventional inverter. This is also observed with the upper and lower boundary depending on modulation index. Second, the spectral envelope magnitude of $V_{\rm CM}$ in the low-frequency band is influenced by $V_{\rm dc}$, f_s, and T_s. Third, slew

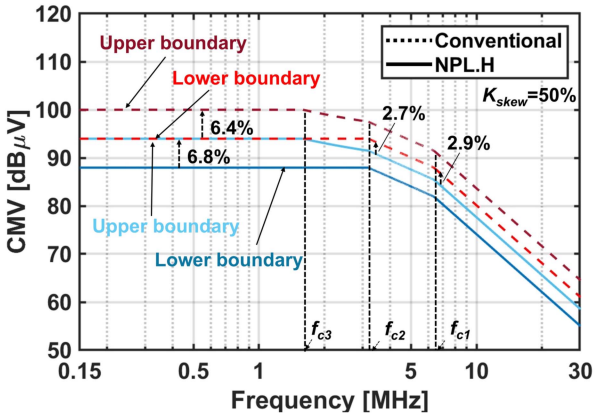

Fig. 7. Analytical spectral envelope of the total CMV considering modulation index at $T_r = 100$ ns, $T_f = 200$ ns, $V_{\rm dc} = 200$ V, $f_s = 5$ kHz, and $K_{\rm skew} = 50\%$.

TABLE I
SPECIFICATIONS OF EXPERIMENTAL SETUP

Specifications		Value
Max. Output Power		25 kW
DC-link Capacitor		200 μF
Switching Frequencies		5–10 kHz
DC-Link Voltages		200–400 V
Part Number		C3M0075120J
Material		SiC
Device Count	NPL.H	18 switches
	Conventional	12 switches

rate disparity affects the spectral envelope of $V_{\rm CM}$ primarily in the high-frequency band rather than the low-frequency band. Lastly, the impact of skewing on active CMV cancellation capability is more significant than that of slew rate disparity in the frequency band (150 kHz–30 MHz).

III. EXPERIMENTAL VALIDATION OF ACTIVE CMV CANCELLATION CAPABILITY IN NPL.H INVERTER

Two inverter prototypes using SiC devices (C3M0075120J) are designed to experimentally assess the active CMV cancellation capabilities of each inverter. To ensure a fair comparison in the EMI analysis, the PCB and inverter hardware layouts, cable lengths, and power level are kept identical. The prototypes include a digital signal processing daughter card, three-phase leg daughter cards, and a dc-link daughter card containing the dc-link capacitors, all mounted on the motherboard. The inverters are connected to two isolated three-phase RL loads, with resistance of 20 Ω and inductance of 7 mH. The maximum output of each inverter was 25 kW. $V_{\rm dc}$ ranging from 200 to 400 V, f_s ranging from 5 to 10 kHz, and 200 μF of dc-link capacitor are utilized, as shown in Table I. The equivalent circuit of each inverter and experimental setup are presented in Fig. 8(a) and (b).

The experimental setup includes a high-voltage power supply, line impedance stabilization networks, a radio frequency current transformer (RFCT), a spectrum analyzer, an oscilloscope, an *RL* load, and the inverters. The RFCT, which has a bandwidth range from 9 kHz to 400 MHz, measures the ground leakage current flowing from the inverter to the ground. The spectrum analyzer, capable of analyzing frequencies up to 2.1 GHz, is used to assess CM EMI noise from the setup. An oscilloscope with a 600 MHz bandwidth and a current probe with a 50 MHz bandwidth is also employed for the measurements. The measured CMVs and ground currents from both the NPL.H inverter and the conventional inverter are analyzed to assess the active CMV cancellation capability of the NPL.H inverter in both the time and frequency domains.

A. Time-Domain Analysis

The line-to-line voltages, a phase current, CMV levels, and ground leakage currents of the conventional inverter and the NPL.H inverter were measured at 200 V $V_{\rm dc}$ and 5 kHz f_s using SVPWM. The line-to-line voltages (V_{ab1} and V_{ab2}) for each inverter is shown in Fig. 8(c), validating three-level and two-level operation, respectively. Due to the multi-level operation of the NPL.H inverter, the phase current ripple during an electrical cycle is reduced by 61% compared to that of the conventional inverter, as seen in Fig. 8(d).

The measured CMV of the NPL.H inverter confirms CMV levels of 0, $\pm V_{\rm dc}/3$, and $\pm V_{\rm dc}/6$, whereas the conventional inverter produces $\pm V_{\rm dc}/2$ and $\pm V_{\rm dc}/6$, as shown in Fig. 8(e). Due to the lower CMV levels in the NPL.H inverter, its $V_{\rm CM}$ magnitude is reduced compared to the conventional inverter. The active CMV cancellation capability of the NPL.H inverter is verified by comparing the $V_{\rm CM}$ measurements, which are 98.9 V for the NPL.H inverter and 200.6 V for the conventional inverter. This results in a 50.7% reduction in the peak-to-peak $V_{\rm CM}$ magnitude of the NPL.H inverter compared to the conventional inverter. Transients in $V_{\rm CM}$ generate ground currents that flow from the inverters to the ground through parasitic capacitors, with the ground current magnitude being directly related to the $V_{\rm CM}$ level. The reduced CMV levels in the NPL.H inverter help mitigate the $V_{\rm CM}$ magnitude by canceling out the CMVs, which in turn reduces the ground current. In the NPL.H inverter, the peak-to-peak ground current magnitude is measured at 0.24 A, while in the conventional inverter, it is found to be twice as large, as shown in Fig. 8(f).

During the actual operation of both inverters, the measured CMVs show that parasitic-induced ringing leads to an expansion in the width of $V_{\rm CM}$. This effect causes the corner frequencies to shift to lower values than those predicted by the analytical spectral suppression, which is based on an ideal trapezoidal waveform. To thoroughly evaluate the active CMV cancellation capability of each inverter, effective parameters (i.e., $T_{s\_\rm eff}$, $T_{r\_\rm eff}$, and $T_{f\_\rm eff}$) are examined.

As the width of $V_{\rm CM}$ varies with the switching states in both inverters, $T_{r\_\rm eff}$ and $T_{f\_\rm eff}$ are measured over each time interval, starting from the onset of the $V_{\rm CM}$ until the ringing subsides. The remaining portion of the width is defined as T_{s_eff}. At 200 V V_{dc} and 5 kHz f_s, the $T_{s\_\rm eff}$, $T_{r\_\rm eff}$, and $T_{f\_\rm eff}$ values for the NPL.H inverter are measured as 2, 3, and 4 μs, respectively, while for the conventional inverter, these values are 0.7, 3, and 4 μs, as shown in Fig. 9(a) and (b). This indicates that the NPL.H inverter

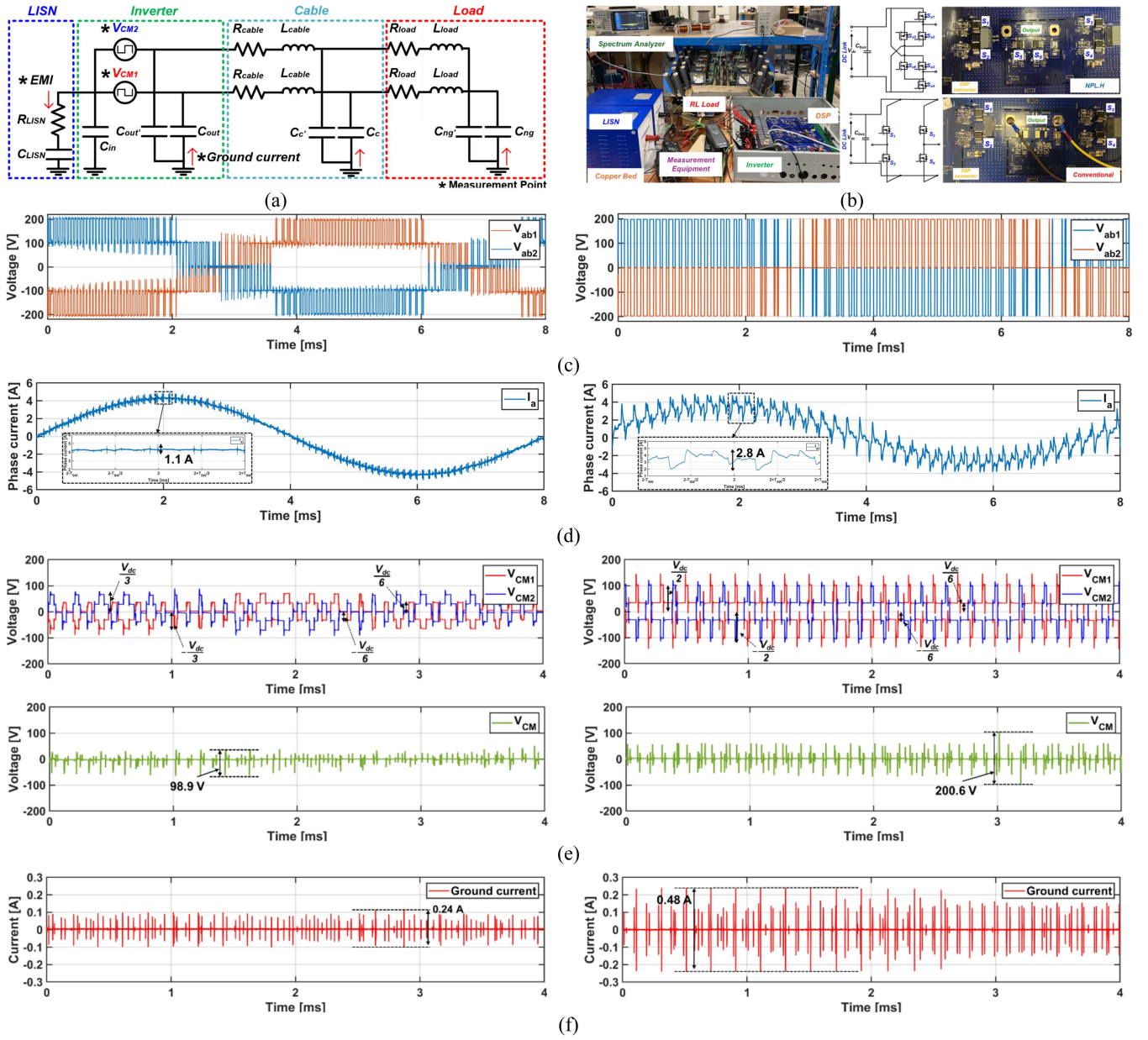

Fig. 8. (a) Equivalent CM circuit of an experimental setup with the measurement points. (b) SiC-based prototypes of each inverter. Measured (c) line-to-line voltages and (d) phase currents in an electrical cycle from each inverter. (e) Measured total residual CMVs and (f) ground currents in a half electrical cycle from each inverter at $V_{\rm dc} = 200$V and $f_s = 5$ kHz.

has a longer settling time compared to the conventional inverter, primarily due to the commutation loop required for multilevel operation. The stray inductance in this loop contributes to the increased $T_{s\_\rm eff}$ in the NPL.H inverter [33]. Additionally, the ringing frequencies observed during switching events in both inverters range from 3 to 12.5 MHz, as determined by the measured ringing cycles of the $V_{\rm CM}$.

B. Frequency-Domain Analysis

As validated analytically in Section III, the disparity effect has a minimal impact on the spectral envelope of the $V_{\rm CM}$ compared to the skewing effect. Therefore, the spectral envelope with the skew ratio is analyzed to verify the experimental results. The frequency spectrum of the $V_{\rm CM}$ for both inverters shows that the magnitudes caused by ringing exceed the analytical envelope in the high-frequency range (3–30 MHz), as shown in Fig. 10(a). With the measured $T_{s\_\rm eff}$, $T_{r\_\rm eff}$, and $T_{f\_\rm eff}$ values for the NPL.H inverter, the measured $V_{\rm CM}$ aligns with the analytical envelope, exhibiting corner frequencies (i.e., $f_{c1} = 0.16$, $f_{c2} = 0.11$, and $f_{c3} = 0.08$ MHz), and $K_{\rm skew}$ is determined to be 67% by $T_{s\_\rm eff}/T_{r\_\rm eff}$. Similarly, the analytical spectral envelope for the conventional inverter, with $K_{\rm skew} = 23\%$, matches the measured V_{CM} frequency spectra, showing corner frequencies (i.e., $f_{c1} = 0.45$, $f_{c2} = 0.11$, and $f_{c3} = 0.08$ MHz).

The measured $V_{\rm CM}$ magnitude in the NPL.H inverter is up to 21% lower than that in the conventional inverter within the frequency band (300 kHz–30 MHz). However, in the frequency band below 0.08 MHz (i.e., f_{c3}), the magnitude in the NPL.H inverter is 2.6% higher than in the conventional inverter, due to the effective skewing time caused by ringing. In addition, the

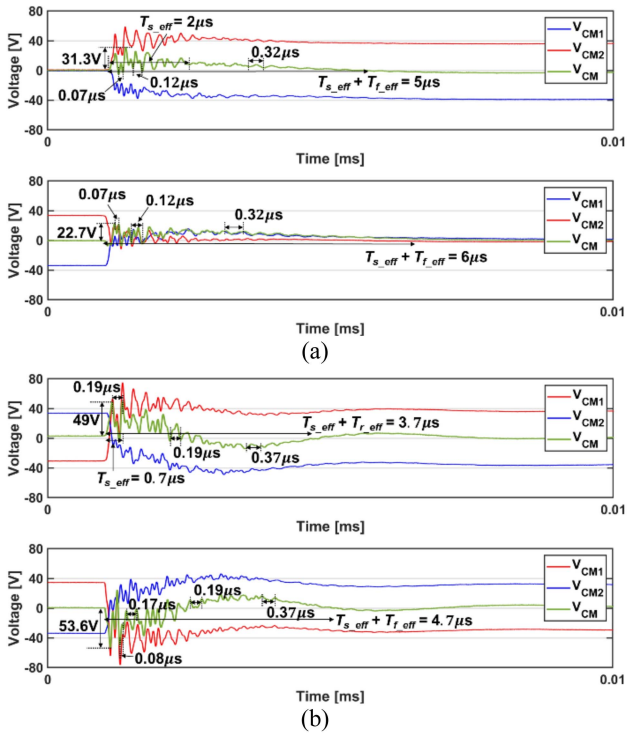

Fig. 9. Measured T_{s_eff}, T_{r_eff}, and T_{f_eff} of CMVs in (a) NPL.H and (b) conventional inverters at $V_{\mathrm{dc}} = 200$ V and $f_s = 5$ kHz.

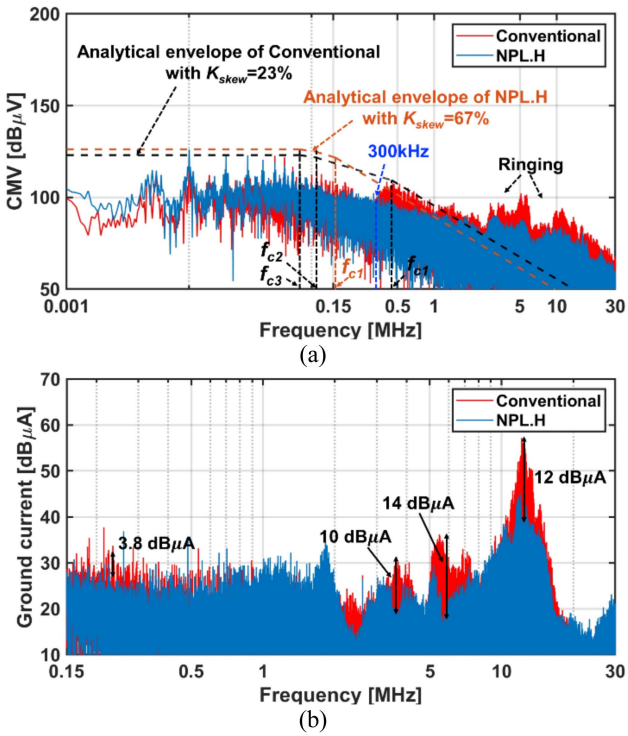

Fig. 10. (a) Frequency spectra of each V_{CM} and (b) ground current in NPL.H and conventional inverters at $V_{\mathrm{dc}} = 200$ V and $f_s = 5$ kHz.

ground currents flowing from each inverter to the ground are compared in Fig. 10(b). The variations in magnitudes between the inverters are more pronounced in the frequency range of 2–20 MHz than in the range of 150 kHz–2 MHz. The difference in ground currents between the inverters is measured at 3.8 dBμA in the hundreds of kHz range, while it increases to 14 dBμA in the MHz range. These results confirm that the active CMV cancellation in the NPL.H inverter significantly reduces the magnitude of CM current flowing from the inverter to the ground, especially at frequencies above 2 MHz, compared to the conventional inverter.

IV. CM EMI Analysis With Active CMV Cancellation

The measured CM EMI noise magnitudes at varying V_{dc} and f_s values are analyzed to validate the correlation between the effectiveness of active CMV cancellation and CM EMI noise magnitude in both inverters. The CM EMI noise magnitudes from the inverters are measured at V_{dc} values of 200 V and 400 V and f_s values of 5 kHz and 10 kHz. For the NPL.H inverter, the CM EMI noise magnitude increases by 4.4 dBμV in the 300 kHz - 2 MHz range and up to 3.4 dBμV in the 2–20 MHz band, as shown in Fig. 11(a). In contrast, under the same conditions, the CM EMI noise magnitude in the conventional inverter at 400 V and 5 kHz increases by 8.4 dBμV in the 300 kHz–2 MHz range and 6.1 dBμV in the 2–20 MHz range, compared to the values at 200 V and 5 kHz.

Similarly, the CM EMI noise magnitude in the NPL.H inverter is elevated by 4.2 dBμV in the 300 kHz–2 MHz range and by 2 dBμV in the 2–20 MHz band, as shown in Fig. 11(b). In contrast, at the same conditions, the CM EMI noise magnitude in the conventional inverter at 200 V and 10 kHz increases by 8.2 dBμV in the 300 kHz–2 MHz frequency range, compared to that at 200 V and 5 kHz and by 5.2 dBμV in the 2–20 MHz band. These results also confirm that the measured CM EMI noise magnitudes exceed the CISPR 22 standard within the 1 to 10 MHz frequency range as V_{dc} increases from 200 to 400 V and f_s rises from 5 to 10 kHz. In contrast, the NPL-H inverter produces CM EMI noise levels below the CISPR 22 standard across the entire frequency range under the same operating conditions.

These findings are consistent with the observation that the active CMV cancellation capability of the NPL.H inverter reduces CMV within the frequency range of 300 kHz to 30 MHz. The NPL.H inverter primarily reduces ground current flowing from the inverter to the ground in the 2 to 20 MHz range. However, the observed reduction in measured CM EMI noise magnitude from 300 kHz to 2 MHz is mainly influenced by ground current flowing from the cable and load to the ground rather than the inverter ground current. Furthermore, the active CMV cancellation feature of the NPL.H inverter leads to an experimentally confirmed reduction in the sensitivity of CM EMI noise magnitude to variations in dc-link voltage and switching frequency within the 300 kHz to 20 MHz range when compared to the conventional inverter.

V. Conclusion

This article analytically and experimentally demonstrated the effectiveness of active CMV cancellation in the NPL.H inverter, which is optimal for balanced six-phase and dual three-phse winding motors. The reduced CMV levels achieved during three-level operation allowed for more effective CMV suppression compared to the conventional inverter, despite mismatch challenges within the NPL.H inverter.

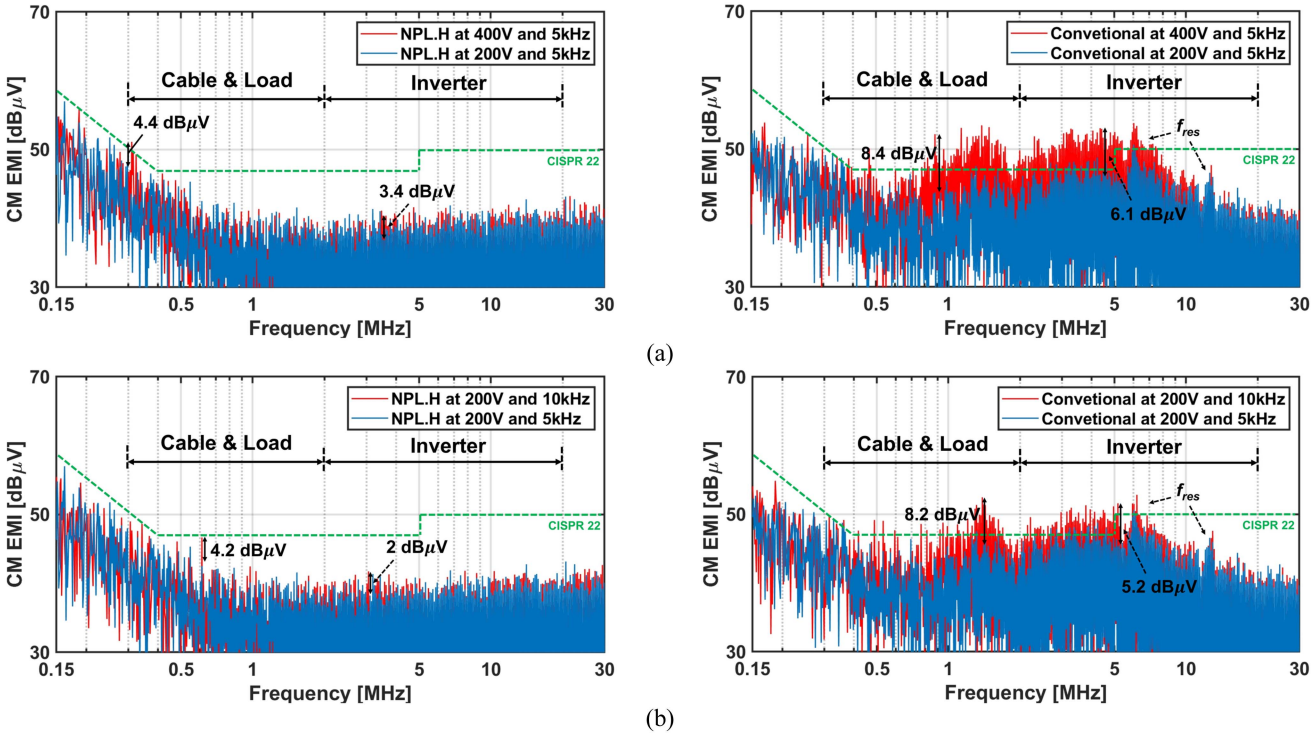

Fig. 11. (a) Measured CM EMI noise magnitudes at $V_{\rm dc} = 200$–400 V and $f_s = 5$ kHz, (b) Measured CM EMI noise magnitudes at $V_{\rm dc} = 200$ V and $f_s = 5$–10 kHz in NPL.H and conventional inverters.

The analytical spectral envelope investigation of residual CMV revealed key insights into the impact of skewing and slew rate disparity between CMVs on cancellation capability. The NPL.H inverter effectively suppresses CMV across the entire frequency spectrum compared to the conventional inverter. The spectral envelope in the low-frequency range is determined by dc-link voltage, switching frequency, and skewing time, while slew rate disparity predominantly influences high-frequency characteristics. In addition, the skewing effect was found to have a more significant effect on active CMV cancellation than the disparity effect.

The measured CMV levels in the NPL.H inverter, consisting of $0, \pm V_{\rm dc}/3$, and $\pm V_{\rm dc}/6$, led to a 50% reduction in peak-to-peak ground current at 200 V dc-link voltage and 5 kHz switching frequency compared to that in the conventional inverter. Although the active CMV cancellation capability in the NPL.H inverter was reduced below 70 kHz due to ringing, the frequency-domain analysis highlighted a 21% reduction in residual CMV within the 300 kHz–30 MHz range. The comparison of ground current magnitudes further indicated that the active CMV cancellation capability of the NPL.H inverter mitigates inverter ground current in the 2 - 20 MHz frequency band compared to the conventional inverter while suppressing noise associated with cables and loads under 2 MHz range.

When dc-link voltage increased from 200 to 400 V, the CM EMI noise magnitude in the conventional inverter rose by 8.4 dBμV in the 300 kHz–2 MHz range and 6.1 dBμV in the 2–20 MHz band. In contrast, the NPL.H inverter limited these increases to 4.4 dBμV and 3.4 dBμV, respectively. Similarly, when switching frequency increased from 5 to 10 kHz, the conventional inverter exhibited noise rises of 8.2 dBμV and 5.2 dBμV in the respective frequency bands, whereas the NPL.H inverter restricted them to 4.2 dBμV and 2 dBμV. These results confirmed that the suppressed CMV magnitudes in the NPL.H inverter effectively mitigate CM EMI noise variations across different operating conditions.

REFERENCES

[1] L. Chang, W. Lee, T. M. Jahns, and K. Rahman, "Investigation and prediction of high-frequency iron loss in lamination steels driven by voltage-source inverters using wide-bandgap switches," *IEEE Trans. Ind. Appl.*, vol. 57, no. 4, pp. 3607–3618, Jul./Aug. 2021.

[2] A. K. Morya et al., "Wide bandgap devices in AC electric drives: Opportunities and challenges," *IEEE Trans. Transp. Electrific.*, vol. 5, no. 1, pp. 3–20, Mar. 2019.

[3] Y. Zhou, W. Chen, and X. Yang, "Investigation of cascade connection method to improve the insertion loss of DM active EMI filters," *IEEE J. Emerg. Sel. Topics Power Electron.*, vol. 10, no. 1, pp. 1084–1094, Feb. 2022.

[4] B. Li et al., "Input voltage feedforward active damping-based input current harmonic suppression method for totem-pole bridgeless PFC converter," *IEEE J. Emerg. Sel. Topics Power Electron.*, vol. 11, no. 1, pp. 602–614, Feb. 2023.

[5] S. Luo, C. Bi, W. Bao, F. Li, and D. Zhou, "Analysis and suppression of common-mode EMI using synchronous pulsed compensation in power electronics," *IEEE J. Emerg. Sel. Topics Power Electron.*, vol. 12, no. 6, pp. 5955–5965, Dec. 2024.

[6] Y. Zhang and D. Jiang, "An active EMI filter in grounding circuit for DC side CM EMI suppression in motor drive system," *IEEE Trans. Power Electron.*, vol. 37, no. 3, pp. 2983–2992, Mar. 2022.

[7] S. Wang, F. C. Lee, D. Y. Chen, and W. G. Odendaal, "Effects of parasitic parameters on EMI filter performance," *IEEE Trans. Power Electron.*, vol. 19, no. 3, pp. 869–877, May 2004.

[8] S. Wang, F. C. Lee, and W. G. Odendaal, "Characterization and parasitic extraction of EMI filters using scattering parameters," *IEEE Trans. Power Electron.*, vol. 20, no. 2, pp. 502–510, Mar. 2005.

[9] S.Wang, R. C., J. D. van Wyk, F. C. Lee, and W. G. Odendaal, "Developing parasitic cancellation technologies to improve EMI filter performance for switching mode power supplies," *IEEE Trans. Electromagn. Compat.*, vol. 47, no. 4, pp. 921–929, Nov. 2005.

[10] S. Wang, Y. Y. Maillet, F. Wang, D. Boroyevich, and R. Burgos, "Investigation of hybrid EMI filters for common-mode EMI suppression in a motor

drive system," *IEEE Trans. Power Electron.*, vol. 25, no. 4, pp. 1034–1045, Apr. 2010.
[11] A. Bendicks, T. Dörlemann, T. Osterburg, and S. Frei, "Active cancellation of periodic EMI of power electronic systems by injecting artificially synthesized signals," *IEEE Electromagn. Compat. Mag.*, vol. 9, no. 3, pp. 63–72, Mar. 2020.
[12] Y. Zhang, Q. Li, and D. Jiang, "A motor CM impedance based transformerless active EMI filter for DC-side common-mode EMI suppression in motor drive system," *IEEE Trans. Power Electron.*, vol. 35, no. 10, pp. 10238–10248, Oct. 2020.
[13] D. Hamza, M. Qiu, and P. K. Jain, "Application and stability analysis of a novel digital active EMI filter used in a grid-tied PV microinverter module," *IEEE Trans. Power Electron.*, vol. 28, no. 6, pp. 2867–2874, Jun. 2013.
[14] J. Ji, W. Chen, X. Yang, and J. Lu, "Delay and decoupling analysis of a digital active EMI filter used in arc welding inverter," *IEEE Trans. Power Electron.*, vol. 33, no. 8, pp. 6710–6722, Aug. 2018.
[15] A. Hota and V. Agarwal, "Novel three-phase H10 inverter topology with zero or constant common-mode voltage for three-phase induction motor drive applications," *IEEE Trans. Ind. Electron.*, vol. 69, no. 7, pp. 7522–7525, Jul. 2022.
[16] J. Li, Z. Hu, Y. Wang, and Z. Chen, "H14 three-level inverter for common-mode voltage suppression," *IEEJ Trans. Elect. Electron. Eng.*, vol. 16, pp. 315–323, 2021.
[17] Z. Zhang and A. M. Bazzi, "Common-mode voltage reduction in VSI-fed motor drives with an integrated active zero-state switch," *IEEE J. Emerg. Sel. Topics Power Electron.*, vol. 10, no. 3, pp. 3371–3382, Jun. 2022.
[18] C. T. Morris, D. Han, and B. Sarlioglu, "Reduction of common mode voltage and conducted EMI through three-phase inverter topology," *IEEE Trans. Power Electron.*, vol. 32, no. 3, pp. 1720–1724, Mar. 2017.
[19] Y. Xiang, X. Pei, M. Wang, P. Shi, and Y. Kang, "An improved H8 topology for common-mode voltage reduction," *IEEE Trans. Power Electron.*, vol. 34, no. 6, pp. 5352–5361, Jun. 2019.
[20] A. Von Jauanne and H. Zhang, "A dual-bridge inverter approach to eliminating common-mode voltages and bearing and leakage currents," *IEEE Trans. Power Electron.*, vol. 14, no. 1, pp. 43–48, Jan. 1999.
[21] H. Zhang, A. V. Jouanne, and S. Dai, "A reduced-switch dual-bridge inverter topology for the mitigation of bearing currents, EMI, and DC-link voltage variations," *IEEE Trans. Ind. Appl.*, vol. 37, no. 5, pp. 1365–1372, Sep./Oct. 2001.
[22] D. Han, S. Li, Y. Wu, W. Choi, and B. Sarlioglu, "Comparative analysis on conducted CM EMI emission of motor drives: WBG versus Si devices," *IEEE Trans. Ind. Electron.*, vol. 64, no. 10, pp. 8353–8363, Oct. 2017.
[23] D. Han, "Conducted common mode electromagnetic interference in wide bandgap semi-conductor devices based DC-Fed motor drives: Challenges and solutions," Ph.D. dissertation, Dept. Elect. Eng., Univ. Wisconsin-Madison, Madison, WI, USA, 2017, pp. 133–160.
[24] D. Han, W. Lee, S. Li, and B. Sarlioglu, "New method for common mode voltage cancellation in motor drives: Concept, realization, and asymmetry influence," *IEEE Trans. Power Electron.*, vol. 33, no. 2, pp. 1188–1201, Feb. 2018.
[25] D. Han, C. T. Morris, and B. Sarlioglu, "Common-mode voltage cancellation in PWM motor drives with balanced inverter topology," *IEEE Trans. Ind. Electron.*, vol. 64, no. 4, pp. 2683–2688, Apr. 2017.
[26] P. Tian, F. Chen, T. M. Jahns, and B. Sarlioglu, "The effect of gate drive resistance on the CM EMI performance of the balanced inverter with asymmetrical parasitic impedance distribution," *IEEE Trans. Ind. Appl.*, vol. 60, no. 6, pp. 9052–9065, Nov./Dec. 2024.
[27] P. Tian, W. Lee, and B. Sarlioglu, "Study of performance of balanced inverter under influence of power loop stray inductance," in *Proc. IEEE Transp. Electrific. Conf. Expo*, 2020, pp. 659–664.
[28] K. Lee, M. Benson, M. Fereydoonian, X. Dong, J. Moon, and W. Lee, "Comprehensive electromagnetic interference analysis of Neutral-point-less (NPL) multilevel inverter with active common-mode voltage cancellation," in *Proc. IEEE Appl. Power Electron. Conf. Expo.*, 2023, pp. 237–243.
[29] K. Lee, M. Benson, X. Dong, J. Moon, and W. Lee, "Common-mode EMI noise analysis of neutral-point-less (NPL) multilevel X-type inverter," in *Proc. IEEE Appl. Power Electron. Conf. Expo.*, 2024, pp. 1014–1020.
[30] X. Dong, M. Benson, K. Lee, L. Yi, W. Lee, and J. Moon, "Three-level: Neutral-point-less H-type 3-level inverter," *IEEE Trans. Power Electron.*, vol. 39, no. 2, pp. 2522–2536, Feb. 2024.
[31] M. Benson, X. Dong, M. Guven, K. Lee, J. Moon, and W. Lee, "Neutral-point-less (NPL) multilevel inverter topology with single DC-link capacitor: H-type inverter," in *Proc. 2022 IEEE Transp. Electrific. Conf. Expo*, 2022, pp. 43–48.
[32] M. Benson, X. Dong, M. Guven, K. Lee, J. Moon, and W. Lee, "Efficiency and DC-link ripple analysis of neutral-point-less (NPL) multilevel inverter with discontinuous pulse width modulations," in *Proc. 2022 IEEE Energy Convers. Congr. Expo.*, 2022, pp. 1–7.
[33] A. Halawa, B. Schuchardt, J. Moon, and W. Lee, "Influence of high-frequency power loop inductance on GaN-based neutral-point-less X-type (NPL.X) three-level inverter," in *Proc. 2024 IEEE Transp. Electrific. Conf. Expo*, 2024, pp. 1–6.

Kangbeen Lee (Student Member, IEEE) received the B.S. degree in electrical engineering from Yonsei University, Seoul, South Korea, in 2016, and the M.S. degree in electrical engineering from Michigan State University, East Lansing, MI, USA in 2023. He is currently working toward the doctoral degree in electrical and computer engineering with Purdue University, West Lafayette, IN, USA

His research interests include partial discharge, electromagnetic interference, WBG-based AC machine drive, and electric machines.

Mikayla Benson (Member, IEEE) received the B.S. degree in mechanical and electrical engineering from Kettering University, Flint, MI, USA, in 2020, the M.S. degree in electrical engineering in 2023, and the Ph.D. degree in 2025 from Michigan State University, East Lansing, MI.

Her research interests include wide bandgap device applications, power converters, and neutral-point-less multilevel inverters

Xiaofeng Dong (Member, IEEE) received the B.S. and M.S. degrees in electrical engineering from the Nanjing University of Aeronautics and Astronautics, Nanjing, China, in 2016 and 2019, respectively, and the Ph.D. degree in electrical engineering from Florida State University, Tallahassee, FL, USA, in 2023.

His research interests include control of grid-tied inverters, onboard electric vehicle (EV) battery charger, and wide bandgap (WBG) devices applications.

Lifang Yi (Member, IEEE) received the B.S. and M.S. degrees in electrical engineering from the Nanjing University of Aeronautics and Astronautics, Nanjing, China, in 2016 and 2019, respectively, and the Ph.D. degree in electrical and computer engineering from Florida State University, Tallahassee, FL, USA in 2023.

Her current research interests include precise in-situ magnetic loss measurement, dc circuit breaker, and capacitive wireless power transfer.

Jinyeong Moon (Senior Member, IEEE) received the B.S. degree in electrical engineering and computer science from the Korea Advanced Institute of Science and Technology, Daejeon, South Korea, in 2005, the M.S. degree in electrical engineering from Stanford University, Stanford, CA, USA, in 2007, and the Ph.D. degree in electrical engineering and computer science with the Massachusetts Institute of Technology (MIT), Cambridge, MA, USA, in 2016.

His research interests include circuit analysis in power conversion, electromagnetics, and renewable energy.

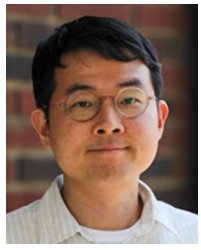

Woongkul Lee (Senior Member, IEEE) received the B.S. degree in electrical & electronics engineering from Yonsei University, Seoul, South Korea, in 2013, and the M.S. and Ph.D. degrees in electrical & computer engineering from the University of Wisconsin-Madison, University of Wisconsin-Madison, WI, USA, in 2016 and 2019, respectively.

In 2024, he joined Elmore Family School of Electrical and Computer Engineering, Purdue University, West Lafayette, IN, USA, as an Assistant Professor. Prior to that, he was an Assistant Professor with Michigan State University, East Lansing, MI, USA. His research interests include high-performance motor drives and distributed energy resources.